JOURNAL OF GEOPHYSICAL RESEARCH, VOL. 94, NO. C3, PAGES 3287–3302, MARCH 15, 1989

Generation of Internal Waves by Sea Ice

MILES G. MCPHEE

McPhee Research Company, Naches, Washington

LAKSHMI H. KANTHA[1]

Program in Atmospheric and Oceanic Sciences, Princeton University, Princeton, New Jersey

Observations in the Greenland Sea marginal ice zone suggest that when strong stratification occurs near the surface, momentum flux into the internal wave field of the upper ocean can be a major component of the force balance that governs ice drift. Since energy is radiated away by the internal waves, turbulent mixing and heat flux are also affected. We investigate the downward flux of momentum and energy by internal waves in an ice-covered ocean, with an idealized model comprising a mixed layer overlying a deep, uniformly stratified layer. A buoyancy jump separates the mixed layer from the pycnocline. Drag from a single wave number component of the under-ice roughness spectrum is derived as the product of a drag coefficient (based on ice speed, under-ice roughness wave number and amplitude, and uniform stratification to the ice-ocean interface) times an attenuation factor that depends additionally on mixed-layer depth and the buoyancy jump at the base of the mixed layer. The model is extended to a plausible spectrum of under-ice roughness by integration over wave number space. Internal wave effects are parameterized in terms of the drag coefficient from the integrated spectrum and incorporated into an upper ocean turbulence model. Model calculations show that plausible values for the peak wave number of the idealized spectrum and roughness variance can account for (1) decreased ice velocity relative to the wind, (2) decreased heat exchange coefficient between the ice and ocean, and (3) lack of mixed-layer deepening, all of which were observed during the last week of the 1984 Marginal Ice Zone Experiment.

1. INTRODUCTION

A nonuniform boundary in motion relative to a stratified fluid generates internal waves which may transfer energy and momentum into the interior of the fluid, bypassing the usual turbulent boundary layer diffusion mechanisms and sometimes drastically increasing the apparent drag of the fluid. *Ekman* [1906] first showed that internal waves caused the hitherto mysterious phenomenon of "dead water," in which ships traversing certain strongly stratified regions experienced a marked increase in power required to maintain low speeds. He demonstrated by elegant laboratory studies how a hull generates large internal waves in stably layered fluids (see, for example, Figure 6-2 of *Gill* [1982]).

There have been extensive studies, including the now classic laboratory experiments of *Long* [1954, 1955], of generation, propagation, and dissipation of internal waves associated with stratified flow over topographic features. A voluminous literature exists for the atmosphere (see, for example, summaries by *Smith* [1979] and *Gill* [1982, chapter 8]), ranging from the effect of internal wave drag on the general circulation (and impact on medium-range weather forecast skill) to clear air turbulence from mountain lee waves. The reader is also referred to *Bretherton* [1969] for an excellent discussion of momentum transport by internal gravity waves.

Generation of internal waves in the ocean by processes near the open ocean surface is much less obvious, although the possible impact of associated momentum and energy flux on mixed-layer dynamics has been noted by a number of authors, including *Kantha* [1977*a*] and *Linden* [1975]. *Kantha* [1979*b*] has discussed turbulent fluctuations in the oceanic boundary layer as a possible source of internal waves in the deep ocean.

In contrast to the open sea, an ice-covered ocean has a ubiquitous source of internal wave generators in the form of pressure ridge keels moving with the wind-driven ice pack. Sea ice motion and polar mixed-layer dynamics are governed in large degree by momentum flux from the ice to the ocean (see, for example, [*McPhee and Smith*, 1976]). The total stress on the ice underside is thought to comprise mainly turbulent "skin friction," associated with Reynolds stress in the shear flow of the turbulent boundary layer plus form drag across pressure ridge keels and other protuberances. The partition of drag between skin friction and form drag is not well understood (see, for example, the discussion in section 1 of *McPhee et al.* [1987]). In addition to turbulence and form drag, downward momentum flux in the internal wave field is also possible; thus a number of investigators have considered the effect of internal wave drag on the force balance of drifting ice. *Hunkins* [1974] extrapolated *Ekman*'s [1906] ship model results to pressure ridge keels and suggested that for commonly observed ice velocities, internal wave drag was small. *Rigby* [1974, 1976] examined keel generation of internal waves, both in theory and experiment, and also concluded that the effect of stress radiation was small unless the ice speed was exceptionally high. Both Hunkins and Rigby considered regimes where the mixed layer was relatively deep, 35–50 m, as is often found in the central Arctic. On the other hand, a carefully executed series of stratified tow tank experiments [*Hachmeister and Rigby*, 1980; *Muench and Hachmeister*, 1984] showed that internal wave drag could be as significant as form drag on ridge keel models under conditions not unlike those found in the

[1]Now at Institute for Naval Oceanography, Stennis Space Center, Mississippi.

Paper number 88JC03974.
0148-0227/89/88JC-03974$05.00

marginal ice zone, where a shallow and strong pycnocline is maintained by surface melting.

The first comprehensive field measurements showing a significant impact of internal wave drag on ice motion came during the 1984 Marginal Ice Zone Experiment (MIZEX '84) near the Greenland Sea ice edge in July 1984. *Morison et al.* [1987] found that during the last week of the experiment, when stratification extended to within a few meters of the ice-ocean interface, the drag coefficient (i.e., the ratio of kinematic stress to the square of relative ice velocity) was 2–3 times as large as the mean value for the entire project. At the same time, the heat transfer coefficient decreased markedly from earlier values. They showed that coherent, high-frequency internal waves were present in the upper 10 m of the water column and demonstrated that their characteristics could account for the increased downward momentum flux. The observations emphasized that internal wave radiation not only modifies the force balance of the ice but also reduces heat and mass transfer at the ice-ocean interface and inhibits mixing, as was shown in laboratory experiments by *Linden* [1975].

The object of this paper is to explore the problem of internal wave generation by moving pack ice. We will be dealing with horizontal scales that are much larger than the scales of the internal waves themselves. Under these conditions, it is possible to regard the ice cover as a homogeneous medium of infinite horizontal extent and to describe statistically both the undersurface of the ice and internal waves generated by the ice cover. This provides a rationale for parameterizing the effect of internal waves in an ice–upper ocean model without resolving the waves directly.

The paper is organized as follows. In section 2 we derive the characteristics of the internal waves generated by ice motion for a single wave number describing the undersurface topography, i.e., for a single Fourier component of the general wave number spectrum of under-ice roughness (or more appropriately, waviness). The effect of a strong density change at the base of the upper layer on wave generation is explored for the general case of a sharp pycnocline separating the upper and lower layers. Expressions for the internal wave drag and the internal wave energy flux are derived.

Section 3 deals with application of the results of section 2 for a plausible spectrum of ice undersurface roughness. The question of equivalent amplitude for a single-wave number roughness is addressed. In section 4 the impact of internal wave drag on the mixed-layer properties is explored with the aid of a one-dimensional mixed-layer model that incorporates first-order closure for turbulence [*McPhee*, 1987] to explain the observations of *Morison et al.* [1987]. Finally, section 5 includes some concluding remarks and recommendations. Appendices A and B deal with extending results to the inertial-internal wave regime and with incorporating the laminar-transition sublayer for heat and mass transfer into the numerical model, respectively.

2. Internal Wave Generation by Ice Motion

In this section we formulate the average momentum and energy flux in the internal wave field in terms of a drag coefficient based on the properties of an idealized system (Figure 1) comprising a "mixed layer" with small or zero buoyancy frequency N_1 and thickness H overlying a deep layer with constant N, all in a rotating reference frame with Coriolis parameter f. Our approach allows for a discontinuous density jump at the interface, signified by Δb (equal to $g\Delta\rho/\rho$). We seek a drag coefficient based on the properties of this system that expresses the ratio of the downward internal wave momentum flux to the square of ice velocity in relation to the undisturbed ocean. The drag coefficient will consist of two factors: (1) a "pure" value c_{wd}, based only on the underlying stratification N, the ice speed U, and characteristics of the ice undersurface (wave number k and amplitude h_0), and (2) an "attenuation factor" Γ that depends additionally on H and Δb. Although Γ will usually decrease the effective drag, we shall also point out that with certain combinations of U, H, and Δb, Γ will be greater than unity, so that drag is actually larger than it would be in the absence of a mixed layer and buoyancy jump.

The governing equation for infinitesimal disturbances in a rotating, stably stratified, Boussinesq fluid (see, for example, *Phillips* [1980] or *Gill* [1982]) is

$$\partial^2/\partial t^2(\nabla^2\bar{W}) + f^2\,\partial^2\bar{W}/\partial z^2 + N^2(z)\nabla_h\bar{W} = 0 \tag{1}$$

where $\bar{W}$ is the vertical velocity and t is time. Subscript h denotes the horizontal component.

Assuming wavelike motions,

$$\bar{W} = W(z)\exp\{i(\hat{k}\cdot\hat{x} - \omega t)\} \tag{2}$$

where $\hat{x}$ refers only to horizontal displacement, ω is the wave intrinsic frequency, and $\hat{k}$ is the horizontal wave number whose magnitude is given by

$$k = |\hat{k}| = (k_x^2 + k_y^2)^{1/2} \tag{3}$$

equation (1) becomes

$$\frac{d^2W}{dz^2} + \begin{bmatrix} N^2(z) - \omega^2 \\ \omega^2 - f^2 \end{bmatrix} k^2 W = 0 \tag{4}$$

Now consider a traveling wave perturbation at the ice-ocean interface ($z = 0$) of the form

$$\bar{W}_S = W_S\exp\{i(\hat{k}\cdot\hat{x} - \omega t)\} \tag{5}$$

caused by motion of the ice cover, as characterized by one particular wave number of the under-ice surface roughness spectrum. We emphasize that we are considering only those wave numbers for which $kh_0 \ll 1$, i.e., with small aspect ratios (since $k = 2\pi/L$, where L is the wavelength of the roughness feature).

We need to match solutions in the upper ($0 > z > -H$) and lower ($-H > z > -\infty$) layers at the interface ($z = -H$). In the upper layer the solution includes both upward and downward propagating waves

$$W_U = W(e^{im_1 z} + re^{-im_1 z}) \tag{6}$$

where r is a reflection coefficient at $z = -H$ and

$$m_1^2 = [(N_1^2 - \omega^2)/(\omega^2 - f^2)]k^2 \tag{7}$$

For the lower layer,

$$W_L = Ce^{imz} \tag{8}$$

where m is the vertical wave number given by

$$m^2 = [(N^2 - \omega^2)/(\omega^2 - f^2)]k^2 \tag{9}$$

Equation (8) has solutions which decay exponentially with depth for $\omega > N$, and wavelike solutions for $f < \omega < N$. We

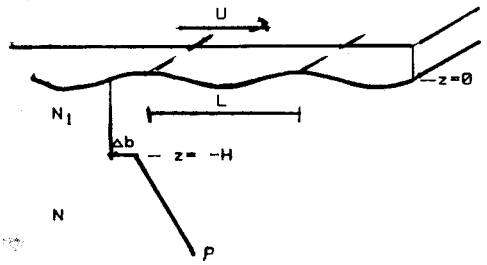

Fig. 1. Schematic of idealized two-layer system with upper layer of small buoyancy frequency N_1 and lower layer with buoyancy frequency N separated by a discontinuous jump Δb. The surface is characterized by sinusoidal relief with wave number $k = 2\pi/L$ and amplitude h_0.

assume that the energy of these waves is directed downward and irretrievably lost from the ice–upper ocean system. This ensures that the wave modes are leaky and can serve as a momentum and energy sink [*Kantha*, 1979*a*].

Matching solutions (6) and (8) at the interface requires continuity of vertical velocity and pressure [*Phillips*, 1980], so that at $z = -H$

$$W_U = W_L \tag{10}$$

$$\frac{dW_L}{dz} - \frac{dW_U}{dz} = \frac{k^2\Delta b}{\omega^2 - f^2} W_L \tag{11}$$

Substituting (6) and (8) and eliminating W and C gives

$$r = \frac{(m_1 - m') \exp(-im_1 H)}{(m_1 + m') \exp(im_1 H)} \tag{12}$$

where

$$m' = m + i\frac{k^2\Delta b}{\omega^2 - f^2} \tag{13}$$

Since the solution at the surface, $z = 0$, is given by

$$W_S = W(1 + r) \tag{14}$$

the solution at the interface, $z = -H$, using (12) is

$$W_I = W_S\left[\cos(m_1 H) + i\frac{m'}{m_1}\sin(m_1 H)\right]^{-1} \tag{15}$$

The upper layer is often well mixed, so with $N_1 = 0$ and $m_1 = i\gamma$ we have

$$W_I = W_S\left[\cosh(\gamma H) + i\frac{m'}{\gamma}\sinh(\gamma H)\right]^{-1} \tag{16}$$

where

$$\gamma = \left(\frac{\omega^2}{\omega^2 - f^2}\right)^{1/2} k \tag{17}$$

Using (13) and (16), the solution at the interface is

$$W_I = W_S\left\{\sinh\left(\frac{\omega kH}{(\omega^2 - f^2)^{1/2}}\right)\left[\coth\left(\frac{\omega kH}{(\omega^2 - f^2)^{1/2}}\right) + i\left(\frac{N^2}{\omega^2} - 1\right)^{1/2} - \frac{k\Delta b}{\omega(\omega^2 - f^2)^{1/2}}\right]\right\}^{-1} \tag{18}$$

which simplifies, for $\omega \gg f$, to

$$W_I = \frac{W_S}{\sinh(kH)[\coth(kH) + i(N^2/\omega^2 - 1)^{1/2} - k\Delta b/\omega^2]} \tag{19}$$

Equation (18) (or (19) for $\omega \gg f$) determines the amplitude of internal waves radiated into the interior as a function of amplitude and wave number of the perturbation at the surface. The system approaches a state of resonance as the term in square brackets approaches zero. Thus, for example, when $f = 0$, the natural frequencies of the system are given by

$$\omega_*^2 = \frac{k\Delta b}{\coth(kH) + i(N^2/\omega_*^2 - 1)^{1/2}} \tag{20}$$

which, for $N = 0$, yields the classical dispersion relation [*Phillips*, 1980] for low-mode internal waves separating two homogeneous layers, the lower being infinitely deep. For nonzero N the solution is more complex and has been investigated by *Kantha* [1979*a*]. The reader is referred to *Kantha* [1979*a*] (especially his Figure 2) for discussions of the wave number–stratification parameter domain for which leaky modes can exist and for other aspects of leaky modes. Briefly, (19) allows for interfacial modes to be leaky and to radiate energy into the interior, a possibly significant factor for maintaining the internal wave climate of the deep ocean [*Kantha*, 1979*a*, *b*]. If a buoyancy jump exists at the interface, we may expect the response of the system to grow as the frequency of the surface perturbation approaches the resonant frequency given by (20).

For the remainder of this section we shall simplify the development by considering high-frequency internal waves ($\omega \gg f$). For completeness the general expression for drag including Coriolis effects is derived in Appendix A and is compared with the nonrotating drag. We find that rotation has a significant effect on drag only for waves with periods close to inertial, which usually contribute little to the overall drag enhancement.

Without rotation the polarization relations may be written

$$\tilde{W}_I = W_I \exp[i(\hat{k}\cdot\hat{x} - mH - \omega t)] \tag{21}$$

$$\tilde{U}_I = -(m/k)\tilde{W}_I \tag{22}$$

$$\tilde{a}_I = (i/\omega)\tilde{W}_I \tag{23}$$

where $\tilde{W}_I$, $\tilde{U}_I$, and $\tilde{a}_I$ are the vertical velocity component, horizontal velocity component, and displacement at the mixed-layer–pycnocline interface, respectively. Note that W_I, given by (18), is a complex quantity.

For $\omega > N$, $\tilde{U}_I$ and $\tilde{W}_I$ are out of phase and therefore cannot contribute to the "wave radiation Reynolds stress"

$$\tau = -\rho\langle\tilde{U}_I\tilde{W}_I\rangle \tag{24}$$

where the average implied by angle brackets is over one wavelength. For $\omega < N$, $\tilde{U}_I$ and $\tilde{W}_I$ remain in phase and the average Reynolds stress is

$$\tau = \frac{\rho/2(N^2/\omega^2 - 1)^{1/2}W_S^2}{\sinh^2(kH)\{[\coth(kH) - k\Delta b/\omega^2]^2 + (N^2/\omega^2 - 1)\}} \tag{25}$$

This stress is the downward momentum flux in the internal wave field and acts in addition to the usual turbulent bound-

ary layer stress. A related quantity is the average downward energy flux

$$\dot{E}_f = (\omega/k)\tau \tag{26}$$

Note that kinetic energy associated with this flux can penetrate deep into the ocean and presumably to locations far from the region where it was generated, whereas the energy associated with turbulence in the boundary layer is dissipated immediately in or near the mixed layer.

For one Fourier component of waviness of the ice undersurface the associated vertical velocity is $W_S = \omega h_0$, and ω is related to ice velocity relative to the undisturbed ocean by

$$\omega = \hat{U} \cdot \hat{k} = Uk_x \tag{27}$$

Here we have aligned the x axis with the direction of ice velocity rather than wave number vector, with no loss of generality. Substituting (27) into (25) and defining a drag coefficient by

$$c_w \equiv \tau/\rho U^2 \tag{28}$$

we have

$$c_w = \frac{1/2(k_x^2 h_0^2)(N^2/U^2k_x^2 - 1)^{1/2}}{\sinh^2(kH)\{[\coth(kH) - k\Delta b/U^2k_x^2]^2 + (N^2/U^2k_x^2 - 1)\}} \tag{29}$$

with k_x less than a critical wave number, $k_c = N/U$. When stratification is uniform throughout the water column ($H = 0$, $\Delta b = 0$), the denominator is unity and the drag coefficient is

$$c_{wd} = \tfrac{1}{2}k_x^2 h_0^2\left(\frac{k_c^2}{k_x^2} - 1\right)^{1/2} \tag{30}$$

The total drag coefficient is $c_w = \Gamma c_{wd}$, with

$$\Gamma = \left\{\sinh^2(kH)\left[\left(\coth(kH) - \frac{k\Delta b}{U^2k_x^2}\right)^2 + \frac{N^2}{U^2k_x^2} - 1\right]\right\}^{-1}$$

$$= \left\{1 + \left[\left(\frac{k_c}{k}\right)^2\left(\frac{k}{k_x}\right)^2 + \left(\frac{k}{k_x}\right)^4 R_b^2\right]\sinh^2(kH) - \left(\frac{k}{k_x}\right)^2 R_b \sinh(2kH)\right\}^{-1} \tag{31}$$

where $R_b = \Delta b/(kU^2)$ is a Richardson numberlike ratio that describes the strength of the buoyancy jump.

For $\Delta b = 0$,

$$\Gamma = [1 + (k_c/k)^2 \sinh^2(kH)]^{-1} \tag{32}$$

Equations (30) and (31) are valid for internal waves for which $f = 0$. The energy flux is

$$\dot{E}_f = \rho U^3 \Gamma c_{wd}(k_x/k) \tag{33}$$

More general expressions for inertial-internal waves (nonzero f) are found in Appendix A.

Disturbances with wavelengths in the x direction less than $2\pi/k_c$ are evanescent and do not contribute to the internal wave stress. We thus consider a nondimensional wave number, $v = k_x/k_c$, and we see that the "pure" drag coefficient (equation (30)) depends only on v and a second dimensionless group h_0k_c:

$$\frac{c_{wd}}{(k_ch_0)^2} = \frac{v}{2}(1 - v^2)^{1/2} \qquad 0 \le v \le 1 \tag{34}$$

as plotted in Figure 2. The function reaches a maximum of 0.25 at $k/k_c = 0.707$ and is nearly linear with slope 0.5 for low values of v. We note that in the nearly linear range of (34), the stress (with no mixed layer) can be expressed simply as

$$\tau \cong \rho\pi h_0^2 NU/L \qquad L \gg 2\pi U/N \tag{35}$$

where L is the wavelength.

In the "dead water" analogy the rapid falloff for v approaching unity coincides with the sharp reduction of drag experienced by a ship as it "outruns" its internal wave wake.

For a specific example, a representative value for k_c during the last phase of the MIZEX '84 drift was 0.3 m^{-1} ($U = 0.1$ m s^{-1}, $N = 0.03$ s^{-1}), so features with wavelengths of 100 m (a fairly typical floe size or ridge separation) yield $v = 0.2$. If the amplitude h_0 is 1 m, the associated drag (with no mixed layer) would be about 9×10^{-3}. This is within a factor of 2 of the drag inferred by *Morison et al.* [1987].

Inspection of (31) shows that the attenuation factor ($\Gamma = c_w/c_{wd}$) depends on three additional nondimensional parameters: k_x/k, kH, and R_b. For simplicity we put $k_x = k$ ($k_y = 0$) in the following treatment and investigate the impact of kH, k/k_c, and R_b. Figure 3 demonstrates how rapidly internal wave drag diminishes with increased mixed-layer depth over a full range of k/k_c. For a wavelength of 100 m the plotted maximum kH of 2 corresponds to about 32 m depth. Thus for a mixed layer with depth as little as 15 m the internal wave drag is only a small fraction of what it would be with no mixed layer. Figure 3 underscores why internal wave drag is not usually a major factor in the ice force balance. However, for a fixed wave number, v varies directly as ice speed, so that as the speed increases, a larger proportion of the energy and momentum flux "tunnels through" a given mixed-layer thickness [see *Gill*, 1982, p. 149].

The effect of a sharp density jump at the base of the mixed layer is examined in Figure 4 for a fixed value of $v = 0.2$. For $U = 0.1$ m s^{-1}, and $k = 0.06$ m^{-1}, a value of $R_b = 6$ implies a density jump of about 0.4 kg m^{-3}. During calm conditions, meltwater can accumulate in a thin layer near the ice, in which case Figure 4 shows that if this stratification becomes strong enough, the ice may initially encounter higher drag than would be expected based on N below the mixed layer. For large R_b and small kH the "attenuation" coefficient may enhance the internal wave drag. The major impact is limited to quite small values of kH, i.e., shallow mixed layers or long wavelengths. For small mixed-layer depths we expect turbulence to erode a sharp density jump fairly rapidly, so that the effect of R_b on drag may not last long.

On the other hand, we do not rule out the possibility that a sharp density interface at intermediate depth may substantially increase the internal wave fluxes into the interior fluid. Consider, for example, conditions representative of the central Arctic late in the melt season [*McPhee*, 1986], with $N = 0.02$ s^{-1}, $H = 20$ m, and $U = 0.2$ m s^{-1}. Figure 5 shows the ratio $\Gamma = c_w/c_{wd}$ as a function of wave number ranging from 0.006 m^{-1} (1-km wavelength) to k_c for zero buoyancy jump (labeled 0.0) and for $\Delta b = 0.002$ m s^{-2} (i.e., salinity changing by 0.25 ppt across a sharp interface at 20 m). It turns out that the latter contains the maximum Δb effect, since the internal Froude number $(U/H\Delta b)^{1/2}$ is 1. The plot shows that in the middle range of wave numbers, $\Gamma_{0.002}$ is 1.5–2 times as large as Γ_0, so that the downward momentum and energy flux is proportionately larger when the density jump is present.

Incidentally, the top panel of Figure 5 also shows dashed

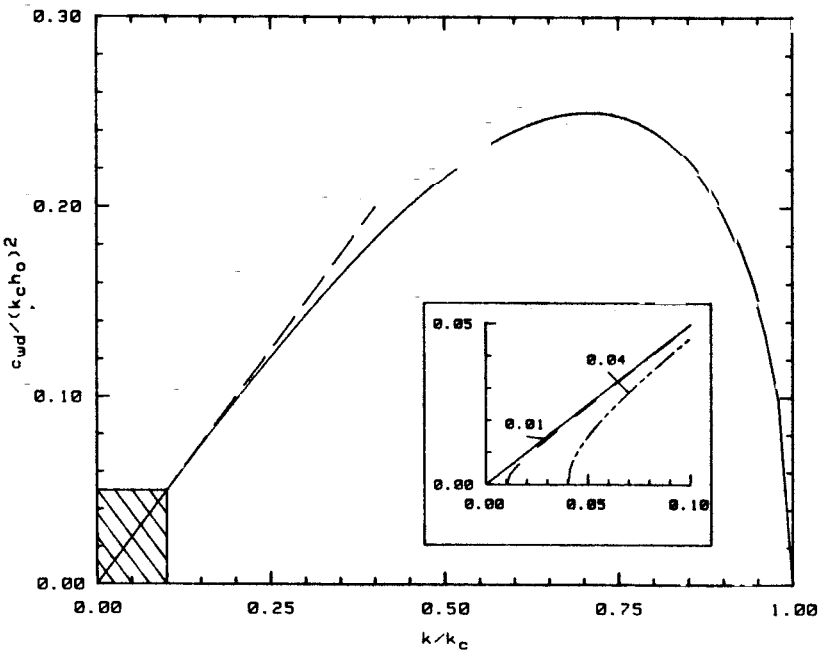

Fig. 2. Drag coefficient scaled by $(h_0 k_c)^2$ as a function of $\nu = k/k_c$, for $H = 0$ and $\Delta b = 0$. The dashed line has slope 0.5. The inset shows the effect of rotation at low wave numbers for f/N equal to 0.01 and 0.04 compared with no rotation. For details, see Appendix A.

lines for which the calculated values of Γ include effects of rotation. The difference is almost imperceptible, except at the lowest wave numbers.

3. Statistical Description of Internal Wave Drag

In this section we use the results from section 2 for a single Fourier component of under-ice roughness to derive the internal wave drag and related quantities for a plausible spectrum of under-ice topography. Actual variations in the ice undersurface range across many scales and in all directions; thus we consider superposition of drag associated with each wave number component in the two-dimensional spectrum of under-ice topographic variance. We write the average drag as

$$\langle c_w \rangle = \int_{\text{all } \hat{k}} c_w(\hat{k})\, S(\hat{k})\, d\hat{k} \qquad \hat{k} = k_x \hat{i} + k_y \hat{j} \tag{36}$$

where, by definition, the variance of under-ice elevation relative to mean draft is

$$\bar{h}_0^{\,2} = \iint_{-\infty}^{\infty} S(\hat{k})\, dk_x\, dk_y \tag{37}$$

We assume that the omnidirectional (i.e., directionally averaged) spectrum $S(k)$ is isotropic, depending only on the magnitude of wave number

$$k = (k_x^{\,2} + k_y^{\,2})^{1/2} \tag{38}$$

Unfortunately, knowledge of the under-ice roughness spectrum, especially at scales important for internal wave generation, is meager. Existing data come mostly from submarines using upward looking sonar; however, relatively few data are available in the open literature (but see, for example, [*Wadhams and Davy*, 1986; *Hibler and LeSchack*, 1972]). *Rothrock*

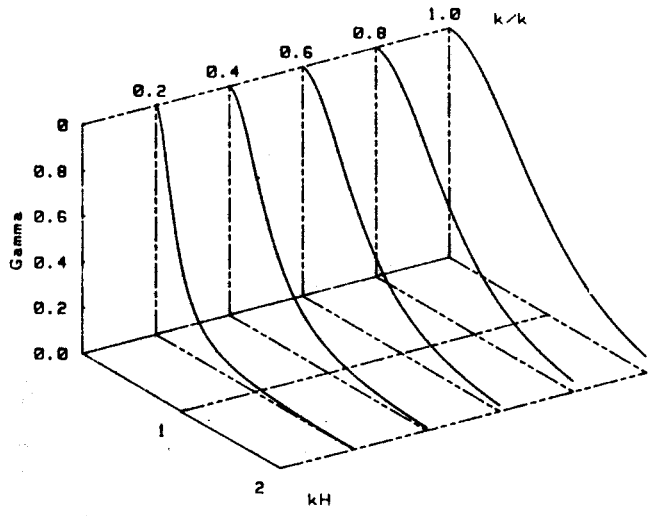

Fig. 3. Ratio $\Gamma = c_w/c_{wd}$ as a function of kH and k/k_c.

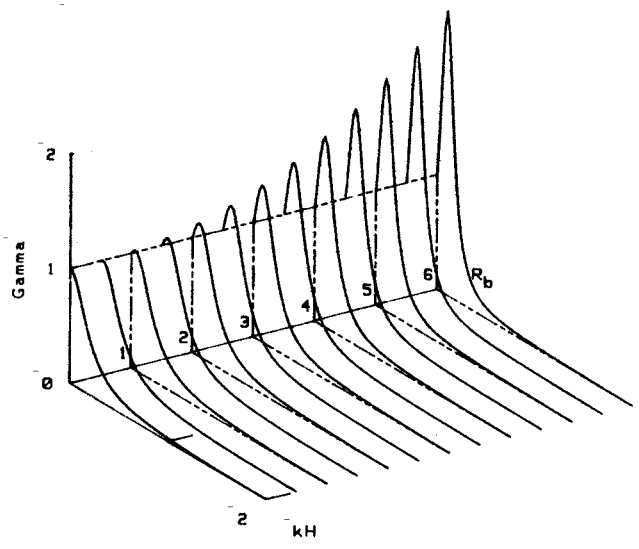

Fig. 4. Ratio $\Gamma = c_w/c_{wd}$ as a function of kH and R_b.

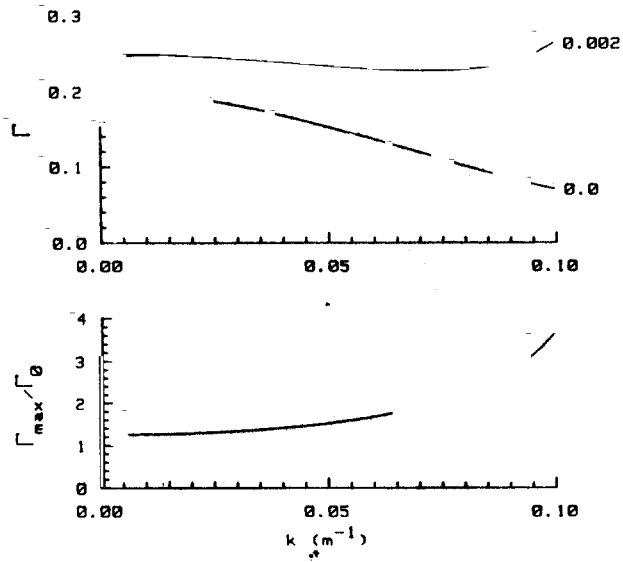

Fig. 5. (Top) Γ versus k for $\Delta b = 0.002$ m s^{-2} and $\Delta b = 0$, for $U = 0.2$ m s^{-1}, $N = 0.02$ s^{-1}, and $H = 20$ m. (Bottom) Ratio of Γ with buoyancy jump to Γ without. Dashed lines (barely visible) indicate the effect of rotation.

and Thorndike [1980] analyzed a 60-km submarine track from the Beaufort Sea and found the one-dimensional spectrum to fall off as k^{-3} at high wave numbers. *McDaniel* [1987] compiled data from several sources and found similar behavior. She also showed that in the range for which the one-dimensional spectrum obeys a negative power law, the omnidirectional spectrum will behave similarly. At low wave numbers, aliasing of the one-dimensional spectrum (from encountering higher-wave number features at oblique angles) makes the correspondence between the one-dimensional and omnidirectional spectra less clear.

In general terms we expect the omnidirectional spectrum to rise from low wave numbers to a broad peak probably associated with the mean floe size distribution and then to fall rapidly at high wave numbers. A simple function with these properties is

$$S(k) = (\bar{h}_0^2/4\pi k_0^3)ke^{-k/k_0} \tag{39}$$

Note that this spectrum is completely specified by the total under-ice variance $\bar{h}_0^2$ and the wave number k_0 at which the peak occurs, since

$$\iint_{-\infty}^{\infty} S(k)\,dk_x\,dk_y = \int_0^{2\pi} d\theta \int_0^{\infty} kS(k)\,dk$$
$$= \frac{\bar{h}_0^2}{2k_0^3}\int_0^{\infty} k^2 e^{-k/k_0}\,dk$$
$$= \bar{h}_0^2 \tag{40}$$

Figure 6 shows this spectrum plotted for unit variance (i.e., $\bar{h}_0^2 = 1$ m^2) on logarithmic axes, along with values in a limited wave number range of the one-dimensional spectrum of McDaniel (her Figure 3) compiled with data of *Rothrock and Thorndike* [1980] and *Mellen* [1966]. We see that the shape of our trial spectrum is similar to the observed one-dimensional spectrum for wavelengths from about 60 m down to 10 m. At higher wave numbers the trial spectrum falls off more rapidly than k^{-3}, but this range is probably not important for internal wave generation.

As with the single wave number component, the effect of our hypothesized spectrum is characterized by a length scale $\bar{h}_0$, which is the root mean square of under-ice elevation deviations, and a wave number at the peak of the spectrum k_0, so that the drag and its attenuation with depth may still be described in terms of dimensionless groups involving $\bar{h}_0$ and k_0. In the following we use angle brackets to distinguish the average drag integrated over the wave number spectrum, $\langle c_w \rangle$, from the drag associated with one wave number component c_w.

Average drag is calculated by two-dimensional, numerical integration using Gaussian quadrature [see *Press et al.*, 1986, chapter 4] of the expression

$$\langle c_w \rangle = \frac{\bar{h}_0^2}{2k_0^2}\int_0^{k_c} dk_x \int_{-\infty}^{\infty} dk_y c_w(k_x)\Gamma(k_x, k)e^{-k/k_0} \tag{41}$$

where

$$c_w(k_x) = \frac{k_x^2}{2}\left(\frac{k_c^2}{k_x^2} - 1\right)^{1/2} \qquad k_x < k_c$$
$$c_w(k_x) = 0 \qquad k_x \geq k_c \tag{42}$$

$$\Gamma(k_x, k) = \left[\sinh^2(kH)\left\{\left(\coth(kH) - \frac{k\Delta b}{\omega^2}\right)^2 + \frac{N^2}{\omega^2} - 1\right\}\right] \tag{43}$$

$$\omega^2 = U^2 k_x^2 \tag{44}$$

The scaled drag coefficient, $\langle D \rangle = \langle c_w \rangle/(\bar{h}_0 k_c)^2$, with H and Δb equal to zero, is drawn in Figure 7 as a function of $\nu = k_0/k_c$, along with the single-wave number function, $D = c_w/(h_0 k_c)^2$, with $k = k_0$. The abrupt cutoff in D at $\nu = 1$ is missing in $\langle D \rangle$ because the spectrum allows contributions from higher wave numbers, with correspondingly higher cutoffs. Similarly, in the middle range of ν the integration includes waves impinging from oblique angles, tending to flatten $\langle D \rangle$ relative to D. Thus one important difference in using a realistic spectrum to compute drag is that the range for which stress varies linearly with speed is reduced to much lower values of k_0/k_c than the corresponding range of k/k_c for the single wave number (Figure 2). For k_0 and N fixed, the speed (since $\nu = k_0 U/N$) at which the ice begins outrunning its internal wake is

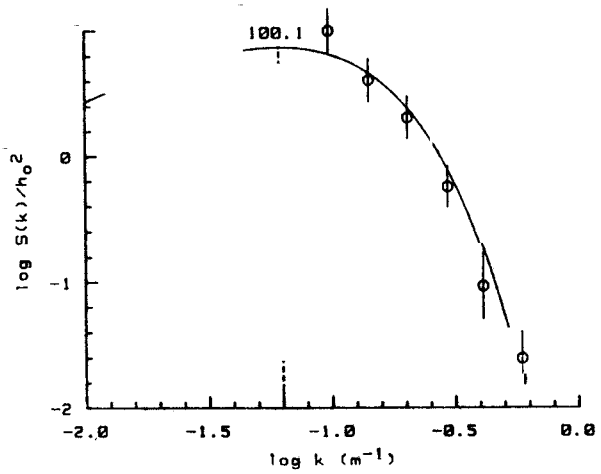

Fig. 6. Trial omnidirectional spectrum normalized by variance. Data points are one-dimensional spectrum of *McDaniel* [1987] plotted with arbitrary vertical offset to compare shapes in limited range. The vertical dashed line indicates the peak of the spectrum, in this case, for $L = 100$ m.

considerably less than would be expected from a single wave number, $k = k_0$. (But note also that with a roughness spectrum, the ice never completely outruns its internal wake.) The drag from a spectrum with given $\bar{h}_0$ and k_0 is considerably less than that from a single wave with the same amplitude and wave number.

Variation of the scaled drag coefficient $\langle D \rangle$ with increasing nondimensional mixed-layer depth $k_0 H$ for $\Delta b = 0$ and various values of v is summarized in perspective view in Figure 8*a*. The corresponding plot of $D = c_w/(h_0 k_c)^2$ for a single-wave number roughness k is shown in Figure 8*b* (note the change in vertical scale). The graphs are made less abstract by considering specific values of k_0 (or k) = 0.06 m^{-1} ($\sim$ 100-m wavelength) and $N = 0.03\ s^{-1}$. The range along the $k_0 H$ axis then represents a range of 0–17 m in mixed-layer depth, while $0 < v < 0.5$ represents a range in ice speed of 0–25 cm s^{-1}.

Since it is much easier to compute drag from a single wave number than by integrating over an entire spectrum, it is pertinent to ask whether we can use an elementary roughness element with wave number $k = k_0$ and amplitude $h_0 = r\bar{h}_0$ to represent the spectrum. We seek a value of r such that $c_w = \langle c_w \rangle$, given by

$$r = h_0/\bar{h}_0 = (\langle D \rangle / D)^{1/2} \tag{45}$$

where c_w is obtained from the simple formulas, (30) and (32).

A plot of r versus v for several values of kH (corresponding to the square root of the ratios $\langle D \rangle / D$ from several planes of Figure 8) is shown in Figure 9. To return to the specific example, for $v = 0.2$ ($k_0 = 0.06$, $k_c = 0.3$) and $kH = 0.13$ ($H \sim 3$ m) we expect h_0 to be about 0.7 $\bar{h}_0$. The main implication of Figure 9 is that as we gain more quantitative knowledge of the under-ice roughness spectrum, we can probably find fairly compact ways of correcting the simple, single-wave number model of ice drag for the effects of a reasonably well behaved spectrum, obviating the need for two-dimensional integration at every estimate of wave drag.

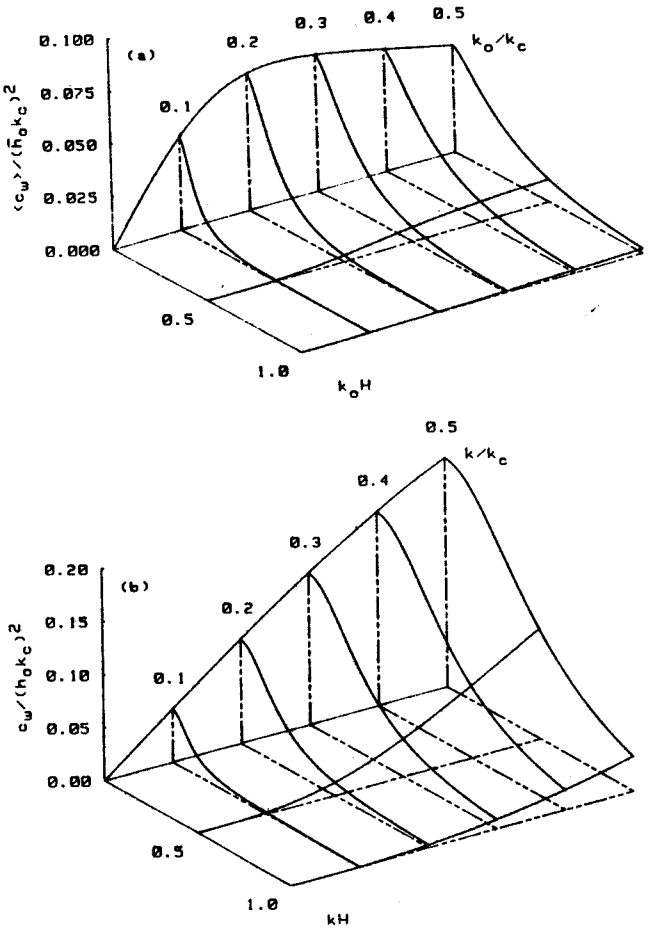

Fig. 8. (*a*) Plot of $< D > = < c_w > /(\bar{h}_0 k_c)^2$ as a function of $k_0 H$ and k_0/k_c for drag integrated over the spectrum of under-ice roughness. (*b*) Plot of $D = c_w/(h_0 k_c)^2$ as a function of kH and k/k_c for a single-wave number roughness.

4. Numerical Upper Ocean Model With Internal Wave Drag

Morison et al. [1987] (hereinafter referred to as MMM) reported conditions during the last week of the MIZEX '84 drift near the Greenland Sea ice edge which suggested that internal wave drag was an important part of the surface momentum balance. In this section we develop a parameterization for the inviscid, two-layer internal wave stress model to be used in a time-dependent, horizontally homogeneous numerical upper ocean model described by *McPhee*

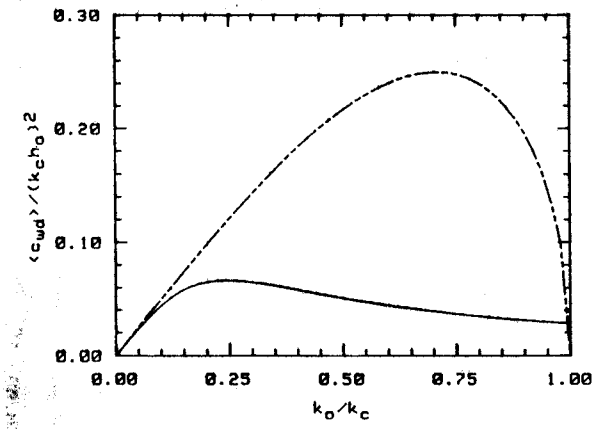

Fig. 7. Plot of $< D > = < c_w > /(h_0 k_c)^2$ versus $v = k_0/k_c$ for $H = 0$ and $\Delta b = 0$ for drag integrated over under-ice spectrum (solid curve) and for drag from single-wave number roughness (dashed curve).

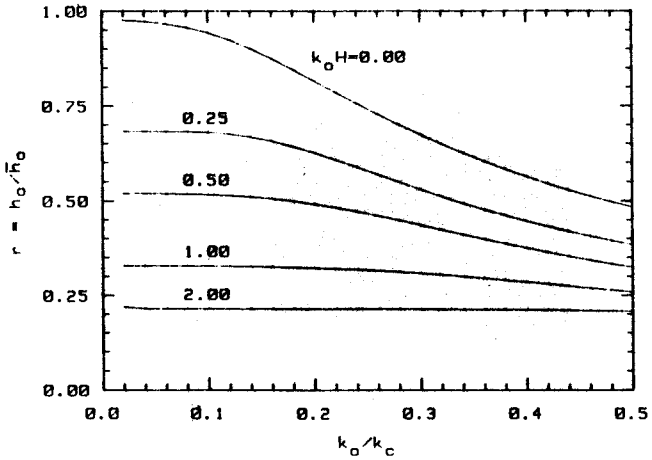

Fig. 9. Ratio $r = h_0/\bar{h}_0$, i.e., where $\bar{h}_0$ is the square root of under-ice roughness variance and h_0 is the amplitude of a single-wave number roughness producing equivalent drag.

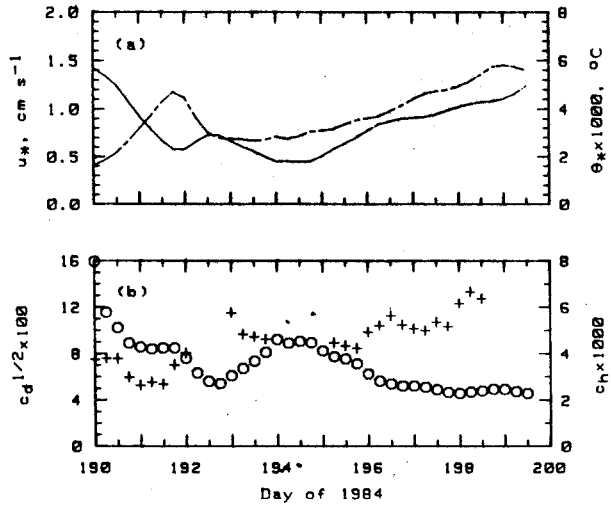

Fig. 10. (*a*) Friction velocity u_* (solid curve) and heat flux temperature scale θ_* (dashed curve) for days 190–200. (*b*) Drag coefficient (plusses) derived from u_* and ice speed relative to 30 m, and heat flux coefficient (open circles) from θ_* and ΔT_{ml}, the departure of mixed-layer temperature from freezing.

[1987]. Our purpose is to test whether internal wave drag can modify the turbulent planetary boundary layer (PBL) model enough to account for the otherwise peculiar behavior described by MMM.

The evidence for internal wave drag is reviewed with the aid of Figure 10 (adapted from Figure 17 of MMM), made from observations of wind stress (indicated by the friction velocity u_* which has been corrected for Coriolis force in the ice), heat flux inferred from ablation of the ice underside, mean ice velocity relative to ocean currents 30 m below the ice, and temperature and salinity of the mixed layer. The heat flux temperature scale θ_* is the kinematic heat flux divided by u_*, i.e., $\theta_* = \langle w'T' \rangle_0 / u_*$, but note that in this case, $\langle w'T' \rangle_0$ is estimated from bottom melt rate, not from direct measurements. The exchange coefficients are defined by

$$c_d^{1/2} = u_*/U_{30}$$

$$c_h = \theta_*/\Delta T_{ml}$$

where ΔT_{ml} is the difference between mixed-layer temperature and the freezing temperature of water with mixed-layer salinity. MMM defined the mixed layer by the depth at which buoyancy frequency exceeded 4 cph (about 0.07 s^{-1}).

Early in the period, u_* was relatively large, but melting was slow because the mixed layer was near freezing. Late on day 190 the floe crossed an oceanic temperature front, and melting increased rapidly as shown by the rise in θ_* (the variables in Figure 10 have been smoothed by a 48-hour filter to make all the time series compatible), accompanied by a decrease in both momentum and heat flux coefficients, attributed by MMM to boundary layer stabilization by surface meltwater. After day 192, winds were weak until day 195, allowing stratification almost to the surface (Figure 11). The period following day 195 is similar to day 191 in terms of surface momentum and heat flux (i.e., u_* and θ_*), but now the drag coefficient is 3–4 times as large, while the heat exchange coefficient is only half as large. If boundary layer turbulence is the only source of oceanic stress, the increased drag is difficult to explain. Stratification inhibits turbulence and tends to confine momentum to a shallower boundary layer; thus we would expect faster drift for the same wind stress (i.e., less drag). In addition, if the added drag were due to increased turbulence levels, we would expect the turbulent heat and salt fluxes to increase as well, and the exchange coefficients would change in concert. By contrast, internal wave (IW) drag drains energy and momentum away from turbulence in the boundary layer, leaving less capacity for direct turbulent overturn and thus lowering the efficiency of the system for heat and mass flux. As was pointed out by MMM, this appears to explain the anomalous exchange coefficients during the last few days of the MIZEX drift.

A quantitative treatment of the effect of internal wave drag on the surface exchange coefficients requires consideration of how the turbulent boundary layer responds to the loss of energy and momentum. As a first cut at the problem, we treat the internal wave stress as an added term in the surface momentum balance of the numerical model. Modeling upper ocean response in a meaningful way during the last week of the MIZEX drift is difficult. Temperature and density fields measured below the moving ice were dominated by advective effects in the complex horizontal gradients of the marginal ice zone (Figures 11 and 12). Successful simulation of upper ocean evolution over the entire period with a one-dimensional (i.e., horizontally homogeneous) model is thus unlikely, and since we lack detailed measurements across an adequate horizontal area at some initial instant (which would have required a massive data collection effort), adding horizontal dimensions to the model would not help. The approach we have taken instead is to make two short (1.5 day) model runs during times when total PBL heat and salt content did not change radically and to consider how the calculated exchange coefficients compare with those observed. The times chosen are indicated by bars in Figure 12 and coincide with the two different exchange coefficient regimes mentioned above.

We use a first-order, time-dependent model for vertical flux of momentum, heat, and salt [*McPhee*, 1987], where turbulent eddy viscosity is proportional to the product of local friction velocity (square root of turbulent stress) and a master length scale that depends on both the rotational length scale u_*/f and the local Obukhov length. The model used here is the same as that of *McPhee* [1987], with the addition of a "laminar-transition" sublayer for heat and mass flux boundary conditions, and the internal wave drag parameterization. Instead of prescribing buoyancy flux at the ice-ocean boundary layer

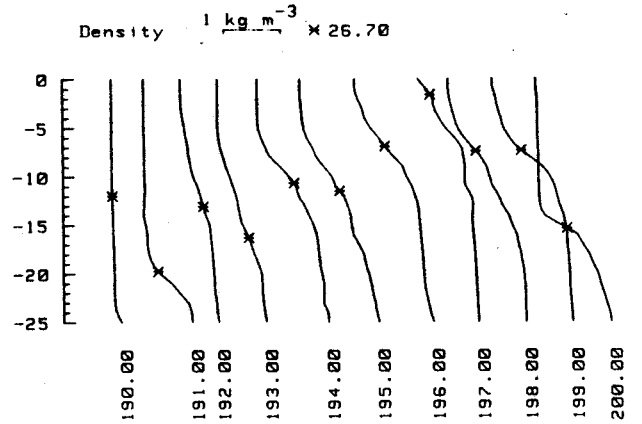

Fig. 11. Density (−1000) in the upper 25 m during the last 10 days of MIZEX '84. Asterisks mark the level at which σ_t is 26.7 in each profile.

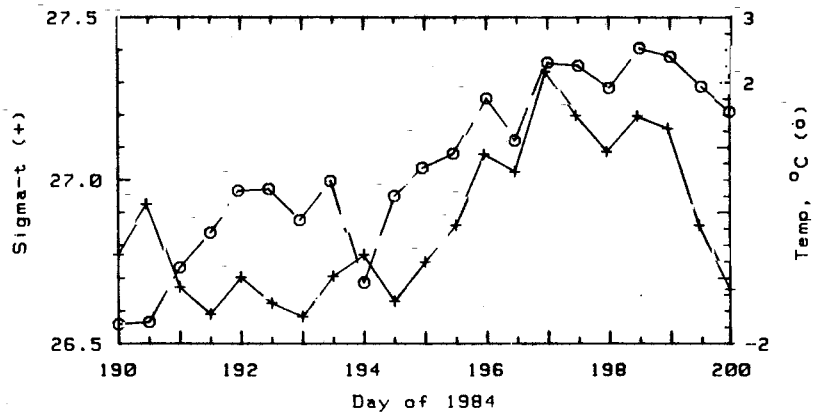

Fig. 12. Average temperature (dashed curve) and σ_t (solid curve) of the upper 25 m for days 190–200. Solid bars indicate 1.5-day periods chosen for modeling.

as in the earlier work, the initial temperature profile is specified, and bottom melting adjusts to turbulent heat flux from the ocean. Subsequent melting both cools and freshens the mixed layer. The "submodel" used for expressing heat flux across the laminar-transition sublayer derives from work by *Yaglom and Kader* [1974] as applied to the under-ice boundary layer by *McPhee et al.* [1987] and is outlined in Appendix B.

Internal wave drag enters the model system as a correction to the dynamic boundary condition (see *McPhee* [1987, section 2.3], except note that the leading term there should be multiplied by ice mass divided by water density)

$$(\rho_i/\rho_0)h\left(\frac{\partial \hat{u}_0}{\partial t} + if\hat{u}_0\right) = \hat{\tau}_a - \hat{\tau}_{IW} - K\frac{\partial \hat{u}}{\partial z}\bigg|_0 \qquad (46)$$

where circumflexes denote vector quantities, with vector magnitude implied when the circumflex is omitted; $\hat{\tau}_{IW} = \langle c_w \rangle u_{ml}\, \hat{u}_{ml}$, $\hat{u}_{ml}$ being the velocity change across the mixed layer, $\hat{u}_0$ is model ice velocity, h and ρ_i are ice thickness and density, ρ_0 is reference water density, $\hat{\tau}_a$ is wind stress divided by water density, and K is model eddy viscosity.

To adapt the inviscid, two-layer model of IW drag to the multilevel numerical PBL model, we must choose criteria for defining the mixed-layer depth H; the buoyancy frequency below the mixed layer, N; and the velocity $\hat{u}_{ml}$. The choices are necessarily somewhat arbitrary, but as long as they are applied consistently they represent another step in the parameterization process. Following MMM, we define the mixed layer in the model by the average depth (greater than 1 m) between the two grid points where the finite-differenced buoyancy frequency exceeds a specified maximum value, 0.01 s^{-1} in this case.

For the critical wave number $k_c = N/u_{ml}$, N is calculated from the density gradient in the 3 m immediately below the mixed layer. Two different schemes were tried. In the first we anticipated that a strong buoyancy jump might develop across the grid cell containing H as defined above. This then became Δb (for use in (43)), with N calculated starting from the lower cell grid point. In the second approach, Δb was set to zero and N was calculated starting from the upper grid point of the cell containing H. As it turned out, neither data nor simulations showed a strong buoyancy jump that was noticeably different from the general buoyancy gradient, so the Richardson number effects discussed in section 2 were always small. Trial simulations showed little difference between the two schemes for calculating N and Δb. Halving the length scale for the density gradient from 3 to 1.5 m also had little impact on model results.

Two methods for determining relative ice/ocean velocity $\hat{u}_{ml}$ were tried. The first was to set $\hat{u}_{ml}$ to model ice velocity, i.e., ice velocity relative to the lowest grid point, which was motionless. In the second method, $\hat{u}_{ml}$ was taken from the vector difference between the ice velocity and current at the first grid point below the mixed layer. The major difference between the two choices lies in the inertial response of the system, as we shall demonstrate later.

An important question regarding the model simulations is whether integrating over a spectrum of under-ice relief is demonstrably different from assuming a single wave number and amplitude for the under-ice topography. Obviously, the latter involves much less calculation and would be preferred where intensive numerical simulation is contemplated. A corollary question is: if a single wave number is sufficient for purposes of modeling ice drift and near surface turbulence levels, then how is its amplitude related to, say, the total variance of the under-ice relief? We address these questions by implementing models for $< c_w >$ given by (29) and by (41)–(43), integrated numerically at each time step.

For the period 197.5–199.0 we present results from four modeling runs. Each run was initialized using temperature and salinity profiles observed at day 197.5 (J. Morison, personal communication, 1986), with initial mixed-layer inertial velocity prescribed following the method of *McPhee* [1987].

TABLE 1. Model Parameters Common to Model Runs 1–6

Parameter	Value
Latitude	81°N
Time step	15 min
10-m wind drag coefficient	0.0023
Model depth	25 m
Vertical levels	50
Undersurface turbulence roughness (z_0)	0.06 m
Initial ice thickness	2 m
Ice salinity	4 ppt
Ice percolation velocity (w_i)	4 cm d^{-1}
Laminar-transition sublayer constant (b)	1.57
Maximum N for mixed layer definition	0.01 s^{-1}
Peak wave number for IW drag model	0.0628 m^{-1}

TABLE 2. Summary of Modeling Results for Runs 1–6 and Observed Data

Run	Comment	$\langle h_0 \rangle$, m	$\langle c_d^{1/2} \rangle$ (×100)	$\langle c_h \rangle$ (×1000)	$\lvert \hat{V}_{in} \rvert$, cm s^{-1}	$\hat{u}_{ice}/\hat{W}$, %/ degree
			Day 197.5–199			
Data			11.88	2.39	5.73	1.44/47.8
Run 1	no IW drag	0.00	5.61	4.31	11.00	2.57/64.7
Run 2	spectrum	2.00	12.48	2.51	7.06	1.41/41.7
Run 3	single wave number	1.40	11.79	2.59	6.38	1.42/40.6
Run 4	$\hat{u}_{ml} = \hat{u}_{ice}$	2.15	12.15	2.49	1.15	.46/26.9
			Day 191.5–193			
Data			7.97	3.42	5.70	1.97/113.9*
Run 5	no IW drag	0.00	6.00	3.81	2.90	2.21/63.0
Run 6	spectrum	2.00	6.96	3.79	2.95	2.19/62.2

$\lvert \hat{V}_{in} \rvert$ is average magnitude of inertial motion from complex demodulation. Complex ice/wind ratio is expressed as percentage (ice speed/wind speed) and angle of rightward deflection in degrees. For observations, $\hat{u}_{ice}$ is with respect to current measured at 30 m.

*During day 192 the ice drifted in an ice edge eddy (see Figure 14 of MMM) which may account for the anomalous angle between wind and ice drift.

All runs were identical (the pertinent model parameters are listed in Table 1), except as follows: run 1, with no IW drag, represents a model "control" case. For run 2, the full spectrum (equation (29)), with $\bar{h}_0 = 2.0$ m and peak wavelength $(2\pi/k_0)$ equal to 100 m, was used to generate IW drag. In run 3, IW drag came from idealized under-ice topography described by a sinusoid of single wave number (wavelength equals 100 m) with amplitude 1.4 m. For runs 2 and 3, $\hat{u}_{ml}$ was taken as ice velocity relative to the current at the first grid point below the mixed layer. Run 4 is similar to run 2 except that $\hat{u}_{ml}$ is model ice velocity and $\bar{h}_0$ is 2.15 m. Results of the model runs are summarized in Table 2.

A comparison among exchange coefficients calculated by the model with and without IW drag (runs 2 and 1, respectively) and MIZEX data is shown in Figure 13. Model time series have been smoothed with a 12-hour filter to remove inertial effects. Dashed curves show average modeled exchange coefficients over the 36 hours, and circles show available observed coefficients from Figure 10. There is reasonable agreement with observations if IW effects increase the momentum exchange coefficient by about 0.07 ($c_w \sim 0.005$), which happens when the total variance of under-ice relief is chosen to be about 4 m^2. Although we lack data on under-ice morphology in the MIZEX '84 region, the value, $\bar{h}_0 = 2$ m, is not unreasonable. From submarine profiles elsewhere, W. D. Hibler (personal communication, 1987) found values ranging from 4 m in heavily ridged ice down to about 1.5 m in smoother ice. From aircraft observations near the MIZEX site, there appeared to be a number of large, multiyear floes in the vicinity, but they were not heavily ridged.

The IW drag model was "tuned" by adjusting $\bar{h}_0$ to give the right increase in total drag, but there are also "predictive" results which are consistent with observations. Most obvious is the close agreement between modeled and observed heat

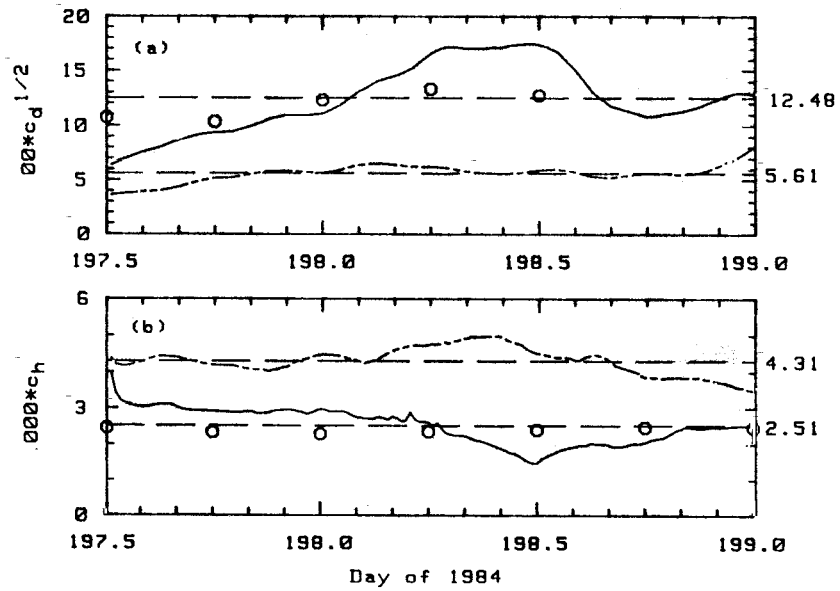

Fig. 13. Time series of (*a*) drag coefficient and (*b*) heat flux coefficient for two model runs, smoothed with 12-hour filter. Solid curves are from run 2 (internal wave drag calculated from spectrum given by (39) with $h_0 = 2.0$ m). Broken curves are from run 1 (same model with no internal wave drag). Average values are indicated by dashed lines and listed at right. Circles are MIZEX data values from Figure 10.

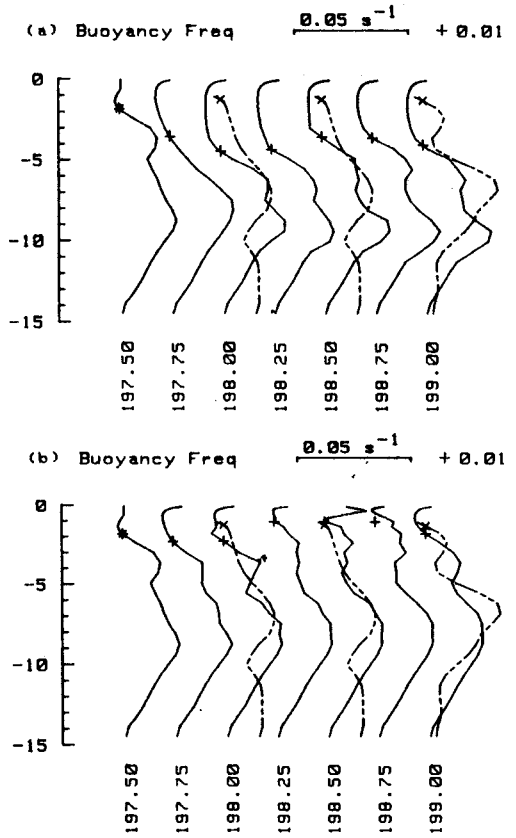

Fig. 14. Profiles of modeled buoyancy frequency (solid curves) for (*a*) run 1 without IW drag and (*b*) run 2 with IW drag. Minimum depth (greater than 1 m) for which N exceeds 0.01 s^{-1} is indicated by plusses. Dashed curves are observed profiles every 12 hours, with mixed-layer depth indicated by crosses.

exchange coefficients (Figure 13). When IW drag is included, the modeled heat exchange coefficient is about 60% of what it would be otherwise. Moreover, since energy is extracted from the system by internal waves, the capacity for mixing and mixed-layer deepening is reduced, as shown in Figure 14. In the model without IW effects (Figure 14*a*) a definite, albeit shallow, mixed layer develops which is absent both in modeled results when IW drag is considered and in the observed profiles. Internal wave drag is sensitive to mixed-layer depth (Figure 8*a*); therefore if mixing is inhibited by internal waves, the effect tends to perpetuate itself. Conversely, once mixing is strong enough to deepen the mixed layer sufficiently, IW stress will decrease, leading to more efficient mixing and more rapid deepening. This in turn will entrain more heat from below, causing enhanced melting and increased surface stratification. The system thus has a number of rather intricate dependencies which are difficult to understand without quantitative modeling.

Ice drift velocity during MIZEX was a complicated mix of wind-driven drift, oceanic geostrophic flow, plus diurnal tidal and inertial oscillations. We estimated velocity relative to the underlying oceanic flow by considering "mean" currents (tidal and inertial signals removed by complex demodulation, see MMM) measured at 30 m depth with a profiling current meter. In Figure 15, ice velocity relative to the 30-m level plus the inertial component determined by complex demodulation of the satellite navigator positions is compared with ice velocity from model runs 1 and 2. Inertial oscillation in the IW drag model is reduced from the control run and seems to correspond roughly with the observed inertial amplitude.

How well IW drag can be modeled using a single-wave number component, vis-à-vis the model spectrum, is addressed by comparing runs 2 and 3, where in run 3 the wavelength is the same as the peak wavelength of the spectrum and wave amplitude is 1.4 m. Results for exchange coefficients are comparable (Figure 16), and although not shown, buoyancy frequency profiles and other responses (Table 2) were similar. A tentative conclusion is that for estimating IW drag, a reasonable spectrum of under-ice elevation deviations may be replaced by a single waveform, with wavelength corresponding to the peak wavelength of the spectrum and amplitude equal to about 70% of the standard deviation of under-ice roughness. For deeper mixed layers this ratio should probably be reduced (Figure 9). Obviously, much additional observational and theoretical/modeling work is needed before this can be stated with confidence.

In run 4, $\hat{u}_{ml}$ was taken to be ice velocity (rather than veloci-

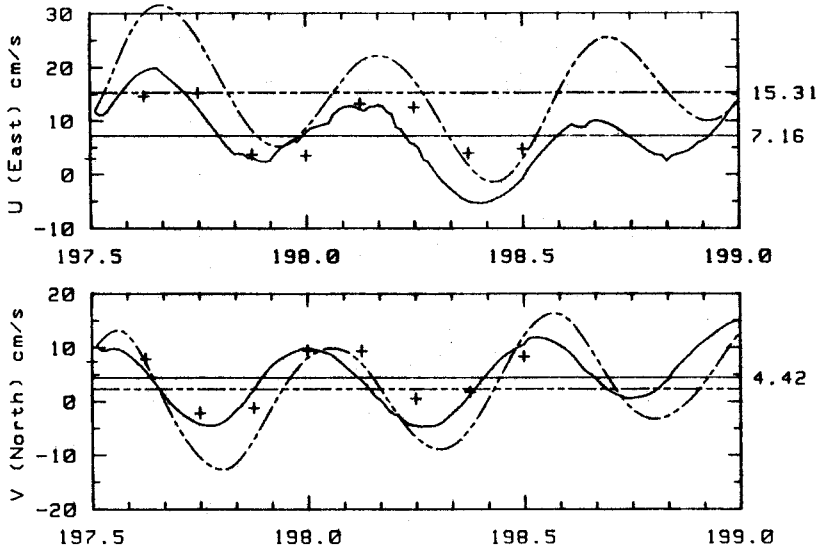

Fig. 15. Velocity components for run 2 (solid curves) and run 1 (dashed curves) with horizontal lines indicating mean values. Plusses are mean ice velocity relative to 30 m plus inertial component of ice motion.

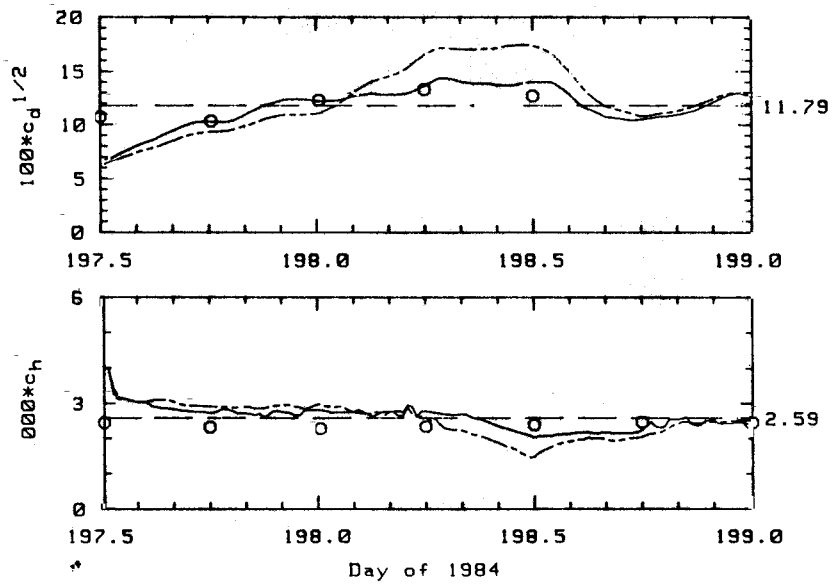

Fig. 16. Same as Figure 13 except solid curves are from run 3 (internal wave drag calculated from single wave number with $k = 0.063$ and amplitude of 1.4 m). Dashed curves are from run 2.

ty difference across the mixed layer) with slightly larger $\bar{h}_0$. Exchange coefficients and density evolution were similar to those in runs 2 and 3, but the difference in modeled surface velocity (Figure 17) shows that inertial oscillations are rapidly damped by fixing the reference velocity to zero. The presence of sizable inertial oscillations in the observed drift and upper ocean currents suggests that the higher-frequency IW interaction responsible for most of the drag takes place with fluid that is also inertially oscillating. The column labeled $|\hat{V}_{in}|$ in Table 2 lists the mean amplitude of inertial motion for each run and the observed amplitude.

The last column in Table 2 lists the complex ratio of the ice velocity vector (relative to surface geostrophic flow) to the wind vector with magnitude, as a percentage, and the angle representing the clockwise drift direction relative to the wind. In addition to a much higher drift/wind percentage when IW drag is neglected (run 1), the deflection angle is about half again as large as the IW drag models and the data.

Finally, runs 5 and 6 demonstrate the IW drag effect during the earlier period (191.5–193), when wind and thermal forcing were roughly comparable to the later period, but stratification was much less pronounced. Run 5 has no IW drag; run 6 uses parameters identical to those in run 2 for the under-ice spectrum. Here we find that IW stress is a minor part of the momentum balance (Figure 18), with lower drag and higher heat exchange than later. Toward the end of the period the ice advected into warmer, more stratified water, unaccounted for in the one-dimensional model. Results from runs 5 and 6 are also summarized in Table 2. During this period the ice drifted across an ice edge eddy (see Figure 14 of MMM), and the 30-m current was affected by geostrophic shear associated with sharp horizontal density gradients near the surface.

5. Conclusions and Recommendations

We have shown how a reasonably simple approach describing internal wave energy and momentum flux in an idealized two-layer system can account for peculiar ice drift conditions during the last part of MIZEX '84, when strong stratification extended almost to the surface. In our formulation the drag coefficient consists of two factors: the drag coefficient that would pertain if uniform stratification typical of the upper pycnocline extended to the ice-ocean interface, and an attenuation factor that depends additionally on mixed-layer depth and the strength of a possible buoyancy jump at the interface.

For a single-wave number component the uniformly stratified drag coefficient is a particularly simple function of the dimensionless wave number kU/N, as given by (34). Rotation modifies the function slightly, as shown in Appendix A; however, the effect is restricted to long wavelengths and probably has little effect on ice drag. The attenuation factor Γ serves to rapidly decrease drag with increasing mixed-layer depth (Figure 3) and explains why internal wave drag is not usually important in the force balance of ice in the central Arctic. In our expression for Γ we include a buoyancy jump Δb as an idealization of the very sharp density gradient often seen at the base of the mixed layer. Under certain conditions, namely when the internal Froude number $U/(H\Delta b)^{1/2}$ is close to 1, the drag coefficient can be substantially increased by the presence of Δb. We demonstrated in section 2 that under conditions typical of late summer in the central Arctic, energy flux into the internal wave field could be as much as doubled if the proper buoyancy jump is present at the base of the mixed layer.

From a qualitative standpoint, considering superposition of drag from an entire spectrum of under-ice waviness does not change much the conclusions of section 2. However, we do find that as the dimensionless wave number k_0/k_c (which for given k_0 and N is proportional to ice speed) increases, the scaled drag coefficient "levels off" much sooner than it would for a single component with wave number k_0 (Figure 7). Consequently, the range of speeds for which stress increases linearly with speed (see (35)) is much reduced when a spectrum of under-ice waviness is considered. Similarly, the abrupt cutoff found for drag from a single-wave number analysis is smeared over higher wave numbers by the spectral integration. The differences between the single-wave number approach and drag integrated over a plausible under-ice spec-

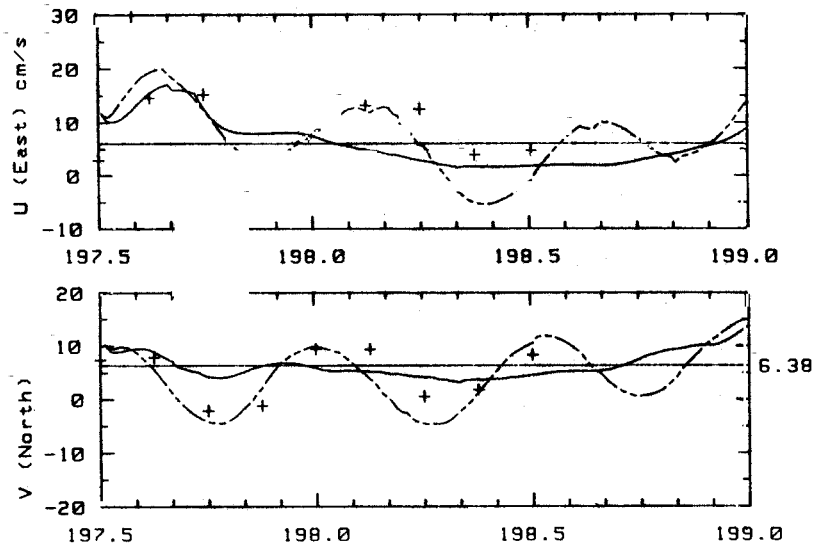

Fig. 17. Same as Figure 15 except velocity components for run 4 (solid curves) and run 2 (dashed curves) with horizontal lines indicating mean values for run 4 (u_{m1} equal to ice velocity). Run 4 overdamps inertial oscillation.

trum for conditions normally expected in the ice-ocean system are summarized graphically in Figure 8.

Regarding the question of using a single-wave number waviness with equivalent amplitude to estimate drag from an integrated spectrum, we find (Figure 9) that the ratio of equivalent amplitude to the standard deviation of under-ice roughness is a weak function of k_0/k_c and a stronger function of k_0H, i.e., the dimensionless mixed-layer depth. A problem for further study is how these dependencies would change under various assumptions about, or quantitative descriptions of, the spectrum of under-ice roughness. In general, we stress that quantitative assessments of the effect of ice motion on the internal wave spectrum of the Arctic Ocean will require many more data on under-ice roughness spectra than are presently accessible.

We have shown by numerical boundary layer modeling how internal wave momentum and energy sinks, represented by our parameterization in the surface momentum balance, can have major impact on near-surface, boundary layer dynamics. We found that by choosing roughness amplitudes which gave the observed total water drag, we could also match rather closely both the observed heat transfer coefficients and the amount of turbulent mixing in the boundary layer. In both cases the results were quite different from a system lacking internal wave flux. The boundary layer calculations were confirmed by also considering a case in which internal wave effects were small because the mixed layer was relatively deep. We point out that IW effects are only one (usually small) aspect of the effect of large-scale roughness features of the ice underside, and that much additional work is needed, for example, to resolve the partition of form drag and turbulent skin friction in the total water stress.

It is also worth noting that we assume that energy propagating out of the ice-boundary layer system is entirely lost (i.e., the leaky modes are perfectly leaky). It is possible that under some circumstances, wave energy might be reflected

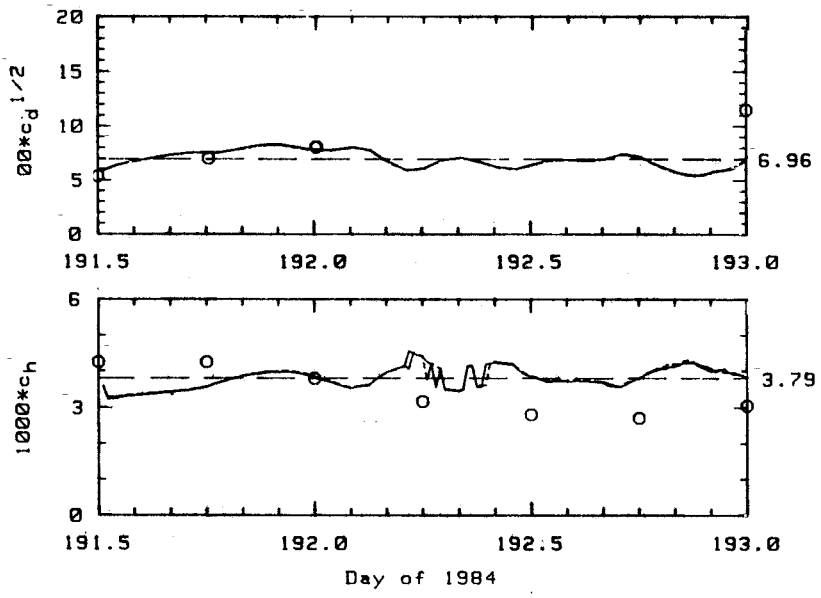

Fig. 18. Same as Figure 13 except solid curves are from run 6 (starting day 191.5, with IW drag) and dashed curves from run 5 (no IW drag).

back from the deep, leading to imperfect leakage and only partial energy and momentum loss. It is therefore appropriate to regard the estimates of wave-induced drag presented here as upper bounds.

A salient feature of the perenially ice-covered Arctic Ocean is the low intensity of the deep internal wave field; energy densities observed under the Arctic ice pack during the Arctic Internal Wave Experiment were an order of magnitude smaller than those observed in mid-latitude oceans [*Levine et al.*, 1987]. Although the ice cover itself is a prime suspect in robbing the internal wave field of its energy, how it does so is not clear. *Morison et al.* [1985] argued that dissipation of internal waves against the ice underside could account for the difference, but it is not obvious to us that interaction of upward-group-velocity internal waves with the strong shear encountered in the wind-driven, rotational boundary layer would be affected much by the presence or absence of sea ice.

There is, however, an almost complete lack of surface gravity wave motion in the interior ice pack. In the open ocean, wind routinely transfers an enormous amount of energy into surface waves, some of which plausibly ends up in the deep internal wave field by resonant generation of internal waves (see, for example, *Kantha* [1977*b*]). This mechanism is supplanted for an ice-covered ocean by the surface topographic generation discussed in this paper. We found the latter to be highly dependent on mixed-layer depth, so that for values typical of the central Arctic (30–50 m), downward energy flux is very small. Thus an alternative explanation for the lower internal wave intensities in the Arctic is that generation by pressure ridge keels cannot compensate for the absence of other surface-based means, such as resonant interaction of surface waves. We note that if such phenomena represent a sizable sink of surface momentum and energy in the open ocean, they will have an impact on mixed-layer dynamics akin to the effects we explored in section 4.

Finally, we find in this work that with stratification conditions found in the marginal ice zone, where rapid melting often occurs, sea ice can become a very effective generator of internal waves, passing a large proportion of the wind stress directly into the internal wave field. In the vicinity of marginal ice zones, which are sometimes quite extensive, especially in the southern ocean, we thus infer that sea ice may be a very significant factor in the local internal wave climate.

Appendix A: Rotational Effects

Here we consider momentum and energy flux from waves with periods of a few hours for which f cannot be ignored. When rotation effects are included in the equations of motion, the horizontal velocity component (equation (22)) is replaced by

$$\tilde{U}_I = -\frac{mk_x}{k^2}\left(1 + i\frac{f}{\omega}\frac{k_y}{k_x}\right)\tilde{W}_I \tag{A1}$$

$$\tilde{V}_I = -\frac{mk_x}{k^2}\left(\frac{k_y}{k_x} - i\frac{f}{\omega}\right)\tilde{W}_I \tag{A2}$$

Vertical velocity and displacement remain the same, i.e.,

$$\tilde{a}_I = i\frac{\tilde{W}_I}{\omega} \tag{A3}$$

$$\tilde{W}_I = W_I \exp\left[i(\hat{k}\cdot\hat{x} - mH - \omega t)\right] \tag{A4}$$

where the expression for W_I is given by (18).

The squared magnitude of W_I is

$$|W_I|^2 = \Gamma_{rot} h_0^2 k_x^2 U^2$$

By defining

$$\beta \equiv \left(1 - \frac{f^2}{\omega^2}\right)^{-1/2} \tag{A6}$$

the rotational counterpart of (31) is

$$\Gamma_{rot}^{-1} = 1 + \left[\frac{k_c^2}{k_x^2} + \beta^2\frac{k^4}{k_x^4}R_b^2\right]\sinh^2(\beta kH) - \beta\frac{k^2}{k_x^2}R_b\sinh(2\beta kH) \tag{A7}$$

For inertial-internal waves there is no equipartition of energy between potential and kinetic components. The average kinetic energy density is

$$E_k = \frac{\rho}{4}|W_I|^2\left[1 + \frac{N^2-\omega^2}{\omega^2}\frac{\omega^2+f^2}{\omega^2-f^2}\right] \tag{A8}$$

while the average potential energy density is

$$E_p = \frac{\rho}{4}\frac{N^2}{\omega^2}|W_I|^2 \tag{A9}$$

so that total energy density is

$$E = \frac{\rho}{2}\frac{N^2-f^2}{\omega^2-f^2}|W_I|^2$$

The vertical component of group velocity is [*Gill*, 1982]

$$c_{gz} = -\frac{(N^2-\omega^2)^{1/2}(\omega^2-f^2)^{3/2}}{(N^2-f^2)k\omega}$$

so that the magnitude of the vertical energy flux is

$$\dot{E}_f = Ec_{gz} = \frac{\rho}{2}|W_I|^2\frac{(N^2-\omega^2)^{1/2}(\omega^2-f^2)^{1/2}}{k\omega}$$

$$= \frac{\rho}{2}\Gamma_{rot}h_0^2k_x^2U^2\frac{N}{k}(1-\nu^2)^{1/2}\left(1-\frac{(f/N)^2}{\nu^2}\right)^{1/2}$$

where

$$\nu = \frac{\omega}{N} = k_xU/N$$

The drag coefficient, from (33), is

$$c_{rot} = \frac{\dot{E}_f}{\rho U^3\Gamma_{rot}(k_x/k)}$$

so that the rotational counterpart of (34) is

$$\frac{c_{rot}}{k_c^2h_0^2} = \frac{1}{2}\nu(1-\nu^2)^{1/2}\left(1-\frac{(f/N)^2}{\nu^2}\right)^{1/2}$$

$$= \frac{\nu}{2\beta}(1-\nu^2)^{1/2}$$

The impact of rotation on the drag coefficient is small, except at small values of ν, as shown in the inset of Figure 2.

The attenuation with depth is also relatively insensitive to rotation for realistic values of k and f, as demonstrated in Figure 5.

Appendix B: Heat and Mass Flux at the Ice-Water Interface

For notation the subscript "1" refers to quantities evaluated at the first grid point in the model, which in our case coincides with $-z_0$, where z_0 is the turbulent surface roughness of the ice underside. Except as noted, the subscript "0" refers to quantities evaluated at the immediate interface, which may be quite different from values at $-z_0$. Salinity flux is

$$< w'S' >_0 = (w_0 + w_i)(S_0 - S_i) \tag{B1}$$

where S_i is ice salinity, w_0 is vertical velocity at the interface due to melting at the interface, and w_i is vertical interface velocity due to melting at the surface or within the ice column. Note that a "percolation" velocity w_i can and often does exist without bottom melting and that a substantial buoyancy flux may occur without much heat flux.

Heat flux is given by

$$< w'T' >_0 = w_0 Q_L + \dot{q} \tag{B2}$$

where $\dot{q}$ is heat conduction per unit mass divided by specific heat, and Q_L is latent heat of melting divided by specific heat and adjusted for brine volume, according to $Q_L = 83.8(1 - 0.03 \times S_i)$ with units of kelvins (or degrees Celsius). We have neglected small changes of specific heat in the first-law balance.

Changes in temperature and salinity from the interface to the first grid point are expressed as nondimensional functions

$$\Phi_T = u_*(T_1 - T_0)/ < w'T' >_0 \tag{B3}$$

$$\Phi_S = u_*(S_1 - S_0)/ < w'S' >_0 \tag{B4}$$

The flux equations may be combined with the freezing line approximation $T_0 = -mS_0$ ($m = 0.054$) to obtain a quadratic expression for S_0:

$$mS_0^2 + [T_q + (1 + c_1)c_2 - mS_i]S_0 - (T_q S_i + c_2 S_q) = 0 \tag{B5}$$

where

$$c_1 = \frac{\Phi_S w_i}{u_*} \qquad c_2 = \frac{\Phi_T Q_L}{\Phi_S}$$

$$T_q = T_1 - \frac{\Phi_T}{u_*}\dot{q}$$

$$S_q = S_1 + c_1 S_i$$

The nondimensional functions Φ_T and Φ_S are discussed by *McPhee et al.* [1987], who suggested the following expressions after considering measurements of turbulent heat flux, temperature, and salinity during the MIZEX drift:

$$\Phi_{T,S} = \frac{1}{k}\ln\frac{|z_1|}{z_0} + b\left(\frac{u_* z_0}{\kappa}\right)^{1/2}\left(\frac{\kappa}{\alpha_{T,S}}\right)^{2/3} \tag{B6}$$

with the empirical constant b equal to 1.57. Here κ is kinematic molecular viscosity, and α_T and α_S are molecular heat and salt diffusivities, respectively.

In the model, surface fluxes of heat and salt are calculated by solving (B5) for S_0 after each time step and calculating w_0, heat flux, and salt flux at the interface. These are then used as boundary conditions for the next time step.

Acknowledgments. We are grateful for the support of this work by the Arctic Programs Branch, Office of Naval Research, under contracts N00014-84-C-0028, N00014-86-C-0438, and N00014-84-K-0640.

References

Bretherton, F. P., Momentum transport by gravity waves, *Q. J. R. Meteorol. Soc.*, *95*, 213–243, 1969.

Ekman, V. W., On dead water, *Sci. Result., Norw. North Polar Exped. 1893–1896*, *5*(15), 152 pp., 1906.

Gill, A. E., *Atmosphere-Ocean Dynamics*, 662 pp., Academic, San Diego, Calif., 1982.

Hachmeister, L. E., and F. A. Rigby, Laboratory studies of stratified flow interaction with topography, in *Proceedings of the Second International Symposium on Stratified Flows*, edited by T. Carstens and T. McClimans, pp. 623–635, Tapir, Trondheim, Norway, 1980.

Hibler, W. D., III, and L. A. LeSchack, Power spectrum analysis of undersea and surface sea-ice profiles, *J. Glaciol.*, *11*, 345–356, 1972.

Hunkins, K., An estimate of internal wave drag on pack ice, *AIDJEX Bull. 26*, pp. 141–152, Univ. of Wash., Seattle, 1974.

Kantha, L. H., Note on the role of internal waves in thermocline erosion, in *Modelling and Prediction of the Upper Layers of the Ocean*, edited by E. B. Kraus, pp. 172–177, Pergamon, Elmsford, N. Y., 1977*a*.

Kantha, L. H., On generation of internal waves in the ocean, *Tech. Rep. 77-3*, Geophys. Fluid Dyn. Lab., Johns Hopkins Univ., Baltimore, Md., 1977*b*.

Kantha, L. H., On leaky modes on a buoyancy interface, *Dyn. Atmos. Oceans*, *3*, 47–54, 1979*a*.

Kantha, L. H., On generation of internal waves by turbulence in the mixed layer, *Dyn. Atmos. Oceans*, *3*, 39–46, 1979*b*.

Levine, M. D., C. A. Paulson, and J. H. Morison, Observations of internal gravity waves under Arctic pack ice, *J. Geophys. Res.*, *92*, 779–782, 1987.

Linden, P. F., The deepening of a mixed layer in a stratified fluid, *J. Fluid Mech.*, *71*, 385–405, 1975.

Long, R. R., Some aspects of the flow of stratified fluids, II, Experiments with a two fluid system, *Tellus*, *6*, 97–115, 1954.

Long, R. R., Some aspects of the flow of stratified fluids, III, Continuous density gradients, *Tellus*, *7*, 341–357, 1955.

McDaniel, S. T., Wave number spectrum of under-ice roughness, *Tech. Memo. 87-145*, 18 pp., Appl. Res. Lab., Pa. State Univ., State College, 1987.

McPhee, M. G., The upper ocean, in *The Geophysics of Sea Ice*, edited by N. Untersteiner, pp. 339–394, Plenum, N. Y., 1986.

McPhee, M. G., A time-dependent model for turbulent transfer in a stratified oceanic boundary layer, *J. Geophys. Res.*, *92*, 6977–6986, 1987.

McPhee, M. G., and J. D. Smith, Measurements of the turbulent boundary layer under pack ice, *J. Phys. Oceanogr.*, *6*, 696–711, 1976.

McPhee, M. G., G. A. Maykut, and J. H. Morison, Dynamics and thermodynamics of the ice/upper ocean system in the marginal ice zone of the Greenland Sea, *J. Geophys. Res.*, *92*, 7017–7031, 1987.

Mellen, R. H., Underwater acoustic scattering from Arctic ice, *J. Acoust. Soc. Am.*, *40*, 1200–1202, 1966.

Morison, J. H., C. E. Long, and M. D. Levine, Internal wave dissipation under sea ice, *J. Geophys. Res.*, *90*, 11,959–11,966, 1985.

Morison, J. H., M. G. McPhee, and G. A. Maykut, Boundary layer, upper ocean, and ice observations in the Greenland Sea marginal ice zone, *J. Geophys. Res.*, *92*, 6987–7011, 1987.

Muench, R. D., and L. E. Hachmeister, Internal wave forces on ice keels in the marginal ice zone: Some preliminary laboratory results, *MIZEX Bull. 3, CRREL Spec. Rep.*, *84-7*, pp. 83–90, U.S. Army Cold Reg. Res. and Eng. Lab., Hanover, N. H., 1984.

Phillips, O. M., *The Dynamics of the Upper Ocean*, 336 pp., Cambridge University Press, New York, 1980.

Press, W. H., B. P. Flannery, S. A. Teukolsky, and W. T. Vetterling, *Numerical Recipes*, 818 pp., Cambridge University Press, New York, 1986.

Rigby, F. A., Theoretical calculations of internal wave drag on sea ice, *AIDJEX Bull. 26*, 129–140, Univ. of Wash., Seattle, 1974.

Rigby, F. A., Pressure ridge generated internal wave wakes at the base of the mixed layer in the Arctic Ocean, master's thesis, Univ. of Wash., Seattle, 1976.

Rothrock, D. A., and A. S. Thorndike, Geometric properties of the underside of sea ice, *J. Geophys. Res.*, *85*, 3955–3963, 1980.
Smith, R. B., The influence of mountains on the atmosphere, *Adv. Geophys.*, *21*, 87–230, 1979.
Wadhams, P., and T. Davy, On the spacing and draft distributions for pressure ridge keels, *J. Geophys. Res.*, *91*, 10,697–10,708, 1986.
Yaglom, A. M., and B. A. Kader, Heat and mass transfer between a rough wall and turbulent fluid flow at high Reynolds and Peclet numbers, *J. Fluid Mech.*, *62*, 601–623, 1974.

L. H. Kantha, Institute for Naval Oceanography; Stennis Space Center, MS 39529.
M. G. McPhee, 1410 Old Naches Highway, Naches, WA 98937.

(Received April 14, 1988;
revised September 19, 1988;
accepted July 1, 1988.)